Chapter 4
Smart Sensor Microsystems: Application-Dependent Design and Integration Approaches

Minkyu Je

Abstract With the future filled with a trillion sensors on the way, there is a large variety in the forms of smart sensors for different applications existing or emerging, such as environmental monitoring, smart grid, green transportation, smart home and building, wearables, implants, and so on. The applications of sensors and corresponding use scenarios define desired form factors, operation frequencies and durations, energy sourcing and management strategies, communication distances and data rates, as well as control interfaces and protocols, leading to significantly different microsystem structures as well as design and integration approaches eventually. In this chapter, the application dependence of the microsystem structures and design/integration approaches are investigated, along with several examples of the smart sensor microsystem implementation across different applications introduced. While we find that the optimally crafted system designs and integration strategies can draw the maximum out of currently available technologies on one hand, the study on the other hand reveals the limitations, challenges, and bottlenecks of the technologies to overcome for a leap to the next stage of the sensor world.

Keywords Smart sensors • Microsystems • Wireless communication • Internet of things • Medical devices • Implantable blood flow sensor • Neural recording • Body-channel communication • Wireless capsule endoscopy • Integrated circuits

4.1 Introduction

Internet of things (IoT), or internet of everything (IoE), has numerous applications already existing or emerging. Such applications include environmental monitoring, smart grid, green transportation, smart home and building, wearables, implants, and

M. Je (✉)
School of Electrical Engineering, Korea Advanced Institute of Science and Technology, 291 Daehak-ro, Yuseong-gu, Daejeon 34141, Republic of Korea
e-mail: mkje@kaist.ac.kr

C.-M. Kyung et al. (eds.), *Smart Sensors and Systems*,
DOI 10.1007/978-3-319-33201-7_4

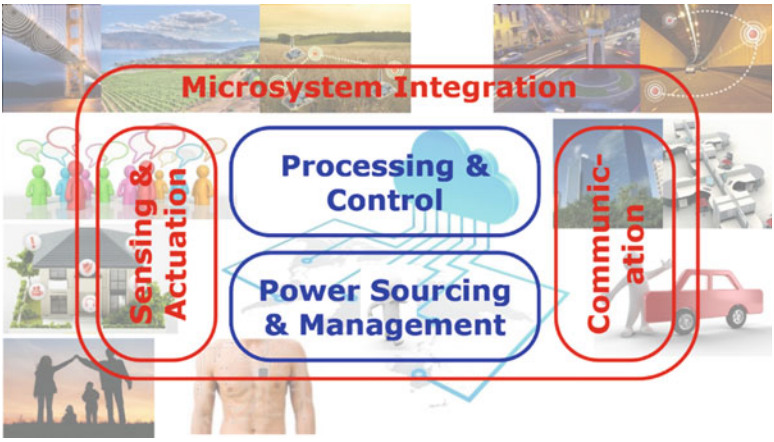

Fig. 4.1 Internet of things (IoT)/IoE (internet of everything) and smart sensor microsystems

so on. From the name, "internet of things," the "internet" means connected cyber world, while the "things" stand for the objects in the physical world. Therefore, implementing IoT means virtualizing physical objects to bring into the networked cyber world. To accomplish this, in the smart sensor microsystem for IoT, we have sensing and actuation function which is necessary for virtualization of physical objects, processing and control function that is also for virtualization, communication function which is for connection, and last but not least, power sourcing and management function which is essential for operating the microsystem. By integrating all these functions, the connected smart sensor microsystem is realized as shown in Fig. 4.1. The aspects of sensing function, communication function, and microsystem integration are mainly investigated in this chapter.

Now, let's look at what are the important factors that are strongly dependent on applications (Fig. 4.2). In the microsystem, its size, lifetime, and physical interface are those factors. In the sensing function, the physical parameters to sense, minimum detection limit, dynamic range, bandwidth, and sensing duty cycles are the application-dependent factors. In the communication function, the communication medium, distance, symmetry, protocol, data rate, and communication duty cycle are such factors. In the following sections, various application-dependent design and integration approaches are investigated and discussed with corresponding examples, mainly in the areas of microsystem integration (Sect. 4.2), sensing (Sect. 4.3), and communication (Sect. 4.4). Then, the conclusion follows in Sect. 4.5.

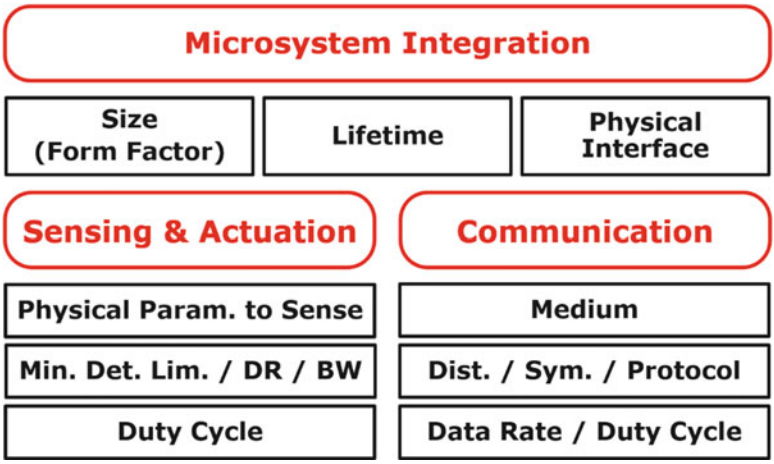

Fig. 4.2 Application-dependent factors in microsystem integration, sensing/actuation, and communication

4.2 Microsystem

4.2.1 Device Size (Form Factor)

The device size or form factor is usually determined by the size of the physical objects where the device is embedded. For example, implants and minimally invasive devices have extreme restriction in their size. In contrast, sensors for smart building and civil structure monitoring don't have much restriction. For wearables, small form factor is important to let users feel comfortable when they wear those devices, but the requirement is not as stringent as the implants and minimally invasive devices.

The size of the device that is constrained by its application in turn determines available capacity of power and energy. Typical primary lithium button cell battery provides 600-mWh energy per cubic centimeter, while rechargeable lithium-polymer cell has the capacity in the range from 250 to 730 mWh per cubic centimeter. Therefore, with current battery technology, if a sensor microsystem of about 1-cm^3 size consumes 1-mW power on average, the microsystem can operate for several hundreds of hours before battery replacement or recharge. If ambient energy sources are tapped to harvest necessary energy for microsystem operation, the power of about 1–100 μW per cubic centimeter is available depending on the kind of sources and environmental conditions (Fig. 4.3 [1]). Consequently, to realize an energy-autonomous microsystem having a form factor less than 1 cm^3, the average power consumption for the overall operation of such a system should be lower than a few microwatts to be on the safe side.

The device form factor also determines microsystem integration scheme. When there is no or little constraint in the device size, the microsystem can be integrated

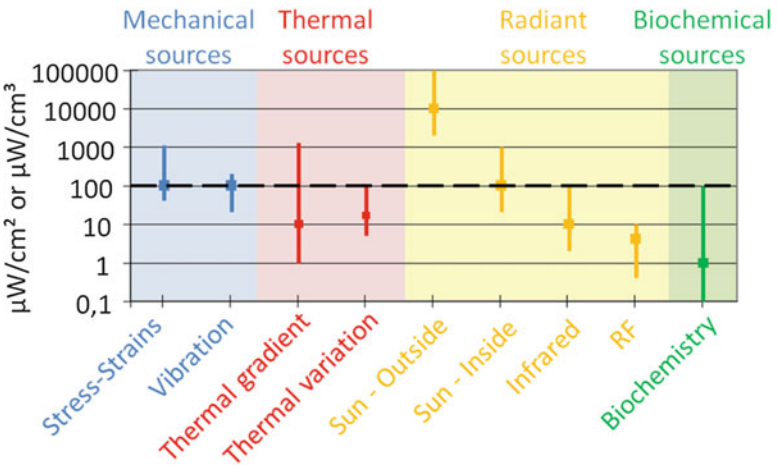

Fig. 4.3 Available power densities from various ambient energy sources [1]

in the form of macromodule. By integrating the microsystem in the form of micromodule, we can make the microsystem form factor much smaller. When there is high restriction in the device form factor, advanced integration technologies have to be used to achieve extreme miniaturization. System-on-chip approach, advanced packaging technology such as wafer-level chip-scale packaging, and 2.5D/3D IC approach based on through-silicon interposer (TSI) and through-silicon-via (TSV) technologies are such integration technologies.

4.2.2 Power Source (or Device) Lifetime

The power source or device lifetime is determined by device usage scenario, accessibility of the installed device, and the number of deployed devices. Since the implant is placed inside a patient's body and surgical procedures are involved to access, its lifetime should be sufficiently long, typically well over 10 years. As the number of sensors in the network grows larger and larger, frequent replacement or recharge of power sources in those sensors will become more and more expensive and eventually impossible. Energy-autonomous sensors will offer nearly infinite lifetime and zero maintenance cost for such large-scale networks. On the other hand, sensors in limited-scale networks that we can find in present smart home and smart building applications, for example, wearable devices, and devices with short-term usage, have less strict requirement on their power source lifetime. Even in those applications of course, longer lifetime is preferred, though not forced.

The required power source or device lifetime determines allowable power consumption and power sourcing/management strategy. For the energy-autonomous sensor node, the average power consumption should be smaller than

the harvested power throughput. When powered by indoor photovoltaic harvesting, for example, the sensor node with a size of 1 cm^3 has to consume the average power lower than 10 μW to achieve energy autonomy, assuming the worst-case harvesting throughput of 10 $\mu W/cm^2$. If the size is 1 mm^3, less than 100 nW should be consumed on average. The implantable cardiac pacemaker with a lithium iodine battery of about 1-Wh capacity should operate with less than 10-μW average power consumption so that the lifetime longer than 10 years can be achieved. To operate the smart watch for longer than 20 h without recharge, the average consumption needs to be lower than 15 mA when it is powered by the rechargeable battery having a capacity of 300 mAh.

4.2.3 Physical Interface with Surroundings

The physical interface of the microsystem with surroundings has to provide an effective isolation barrier between the device and the surroundings to protect one against the other. Hermetic encapsulation isolates the implantable device from surrounding fluid or protects the MEMS sensors against dirt, moisture, and ambient pressure when the sensor is designed to operate in vacuum. Biocompatible packaging is an essential requirement for the implants and on-body devices to minimize the foreign body response and harmful effects on surrounding tissue and cells. Sometimes the package provides EMI shielding if the device operation and performance are sensitive to electromagnetic interference. The MEMS microphone is such an example.

While the effective isolation barrier is constructed on one hand, a proper interface with the surroundings for sensing and actuation has to be provided on the other hand. To do so, controlled minimal exposure of sensors or actuators to the surroundings needs to be implemented somehow, as being done for implantable electrodes, probes, and sensors. For gas sensors, biosensors, and MEMS microphones, proper inlet and guiding microstructures for air and fluid need to be embedded.

4.2.4 Example: Implantable Blood Flow Sensor

The example of application-dependent microsystem integration to investigate is the wireless blood flow monitoring microsystem integrated with a prosthetic vascular graft [2–4]. Prosthetic vascular grafts are widely used for a large number of patients. 20–30 % of the existing renal hemodialysis population has a prosthetic vascular graft in situ, and at least 20 % of bypasses for upper/lower limb ischemia require the use of prosthetic grafts. However, prosthetic grafts are prone to developing progressive stenosis, thrombosis, and ultimately graft abandonment. By monitoring the blood flow rate inside the graft frequently, early stage problem

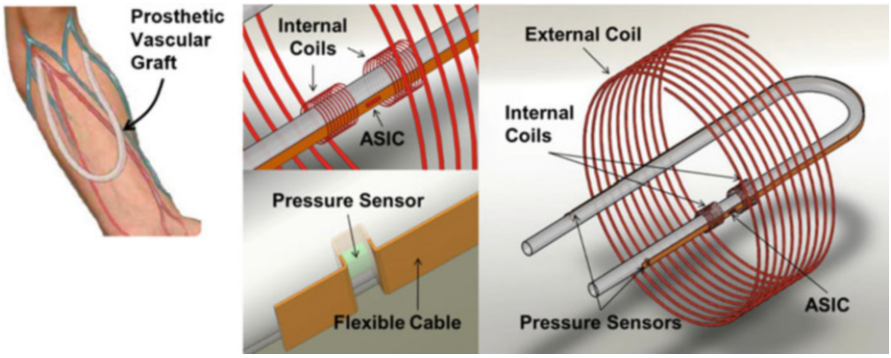

Fig. 4.4 Design and integration approaches of the implantable blood flow monitoring microsystem embedded in the prosthetic vascular graft [2]

detection and intervention can be exercised to prevent graft failure. There exist a few intravascular flow sensing methods such as ultrasound, CT scan, and angiogram. However, they entail morbidity, excessive time and cost, and/or require nephrotoxic contrast, making them ill-suited for frequent monitoring of intravascular blood flow rate.

An implantable wireless blood flow monitoring microsystem embedded in the prosthetic vascular graft provides the most ideal way to frequently monitor the blood flow rate in the graft, when it is paired with an external hand-held monitoring device. Since the microsystem should be integrated within a prosthetic graft, extremely small form factor is required without any room for a battery. The lifetime should be very long as the power source or device replacement incurs a surgery. Since the device is placed inside the human body, biocompatibility is an important concern, while some exposure to the surroundings is also required to sense internal blood flow rate.

Figure 4.4 shows the microsystem design and integration approaches [2]. Since there is no room for battery, we employ passive sensing scheme, where powering the microsystem is accomplished through coil coupling between the implant and the external readout module. The microcoils inside the implant can be placed between the inner and outer layers of the graft. One ASIC, two pressure sensors, and two microcoils are connected using long flexible circuits which can be mounted on the surface of the inner layer. The blood flow rate can be monitored by calculating the difference of the pressure readouts from two pressure sensors located near two ends of the graft. There are minimal incisions at the inner layer to make the pressure sensors exposed to the internal blood stream. The pressure sensors are membrane type rather than cantilever type to avoid endothelialization when exposed to the blood stream. The sensed data are transmitted to the external module through coupled coils by backscattering.

A block diagram of the blood flow monitoring system comprising an implantable microsystem and an external monitoring device is shown in Fig. 4.5 [2]. The microsystem is composed of three key functional subsystems: power link, command/data link, and sensor interface.

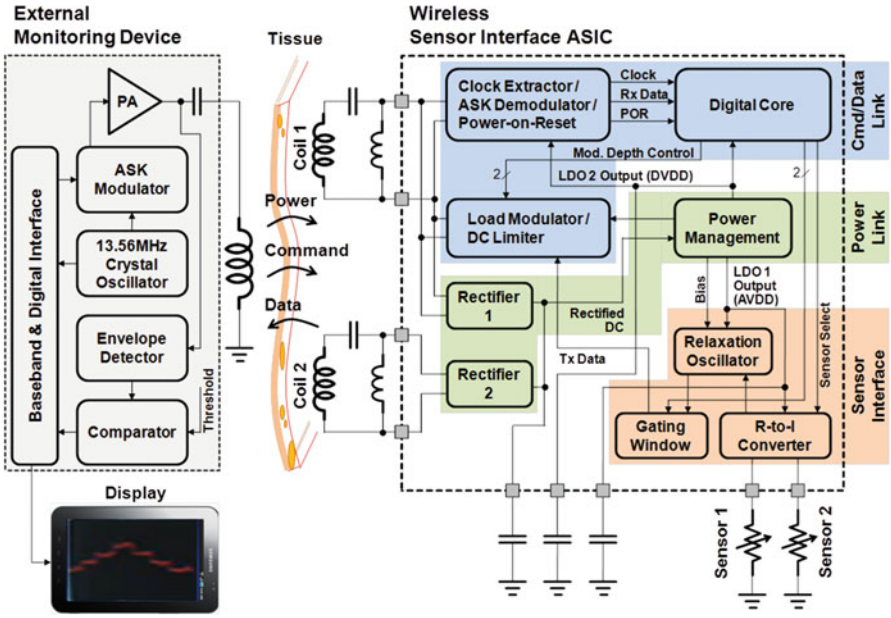

Fig. 4.5 System block diagram of the blood flow monitoring microsystem [2]

- *Wireless power link*: It has two coupling coils, two rectifiers, and a power management block employing low-drop-out voltage regulators (LDOs). The AC power delivered from the primary coil to the secondary coil is converted to the DC power by the rectifiers, which is then regulated by the LDOs to be supplied to circuit blocks in the microsystem.
- *Wireless command/data link*: The command is transmitted using amplitude-shift keying (ASK) with a carrier. After receiving this ASK-modulated RF signal, a clock is extracted from the carrier by a clock extractor and, a power-on-reset (POR) signal is generated to reset the system at the beginning of each measurement cycle. The command is then demodulated by an ASK demodulator. After the microsystem is configured in accordance with the demodulated command, the sensing operation starts. In each measurement cycle, the resistance values of the two pressure sensors are measured in a time-multiplexed manner. The measured resistance values are translated into oscillation frequency by the sensor interface circuit and transmitted to the external monitoring device through backscattering using load-shift keying (LSK).
- *Sensor interface*: The blood flow rate is measured from the difference of pressures sensed by the two MEMS sensors placed at opposite ends of the flexible cable. The piezoresistive sensor transduces the change of the pressure applied on its diaphragm into the resistance change. A sensor interface based on a current-controlled relaxation oscillator is employed to directly translate the resistance value to the oscillation frequency (or the number of counts during a

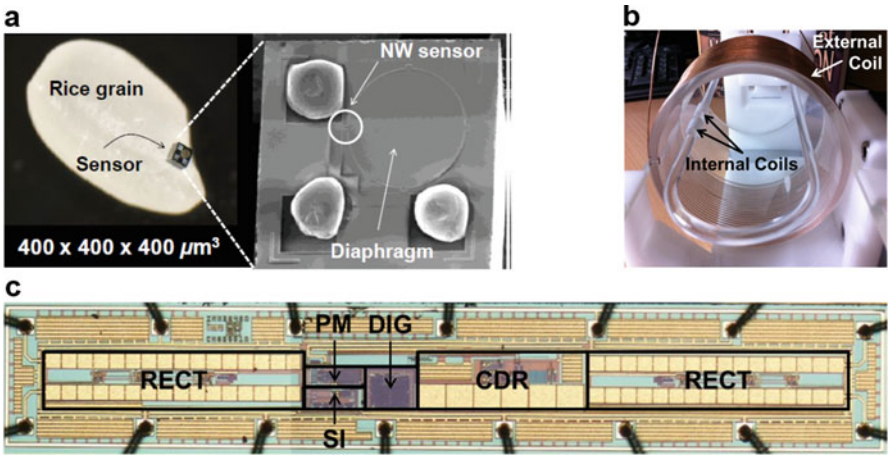

Fig. 4.6 Implementation results of key components [2]: (**a**) MEMS pressure sensor, (**b**) power coupling coils, and (**c**) integrated circuits

predetermined time window). The sensor interface circuit consists of a resistance-to-current converter, a relaxation oscillator, and a gating window control circuit. This approach can greatly simplify the sensor interface design and minimize the power consumption.

The implementation results of key components are shown in Fig. 4.6 [2]. The pressure sensor is made of a silicon nanowire piezoelectric sensor embedded in diaphragm structure. It has an extremely small form factor of $400 \times 400 \times 400\ \mu m^3$, while providing a good sensing performance. For coupling coils, the external coil connected with the readout module is designed to surround the limb. The implanted miniature coils have a diameter of 6 mm. When they operate through 5-cm-thick tissue, the power coupling efficiency is 4.3 %. The integrated circuits support all the necessary functions for microsystem operation, consuming only 12.6 μW.

The results of microsystem integration and wireless sensing test are shown in Fig. 4.7 [2]. To integrate the microsystem within the prosthetic graft, 20-cm-long flexible circuits are mounted on the graft surface and they are coated with the outer layer. The set of materials used for fabricating this new smart graft is the same as that used in the conventional grafts, which is proven to be biocompatible. When the microsystem is tested through 5-cm-thick pork meat as transmission medium, the overall sensing resolution of 0.17 psi is obtained. Importantly, only 600-μW transmission power is sufficient to operate the sensor microsystem, which is possible because of low power consumption and high-efficiency power transfer achieved by the microsystem. It is the very low-level transmission posing no risk of harmful effects on the patient's body.

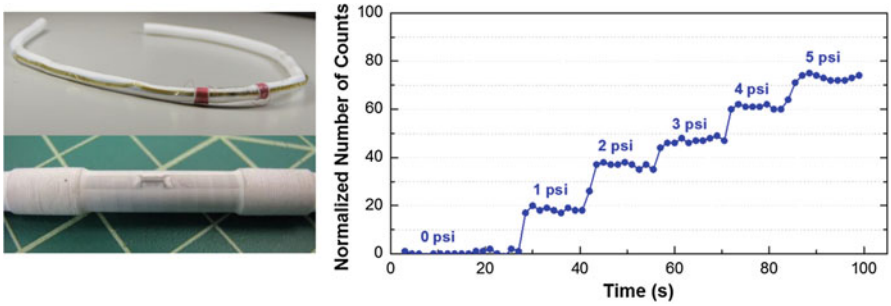

Fig. 4.7 Results of microsystem integration and wireless sensing test

4.3 Sensing

4.3.1 Physical Parameters to Sense

For different applications, different physical parameters need to be sensed for virtualization of "things." The parameters usually sensed are physical forces (e.g., pressure, vibration, acceleration, angular velocity, flow, and tactile force), particles, ions, chemicals, molecules, temperature, humidity, light, potential, and current. To sense different physical parameters, different sensors and corresponding interface circuits are used.

The sensors transduce the physical parameters of interest into electrical quantities. The type of the sensor used determines in which electrical quantity the sensor output is. For example, capacitive accelerometers and pressure sensors are widely used and generate the output in the form of capacitance. Piezoresistive force sensors transduce the physical force into the resistance output. The output of biopotential electrodes and piezoelectric force sensors is in the form of electrical voltage. Ion-sensitive field-effect transistors (ISFET) and optical sensors generate current output.

4.3.2 Minimum Detection Limit, Bandwidth, and Dynamic Range

The minimum detection limit required for the sensing function is determined by the intrinsic strength of the signal that needs to be sensed, the distance from the signal origin, and the signal level of interest. Recording of various biopotential signals illustrates these points very well (Fig. 4.8). Local field potential (LFP), electrocorticogram (ECoG), and electroencephalogram (EEG) have the same signal origin. But the signal amplitudes are not the same as the distance between the location we record and the origin of signal is different. The closer to the origin, the larger the

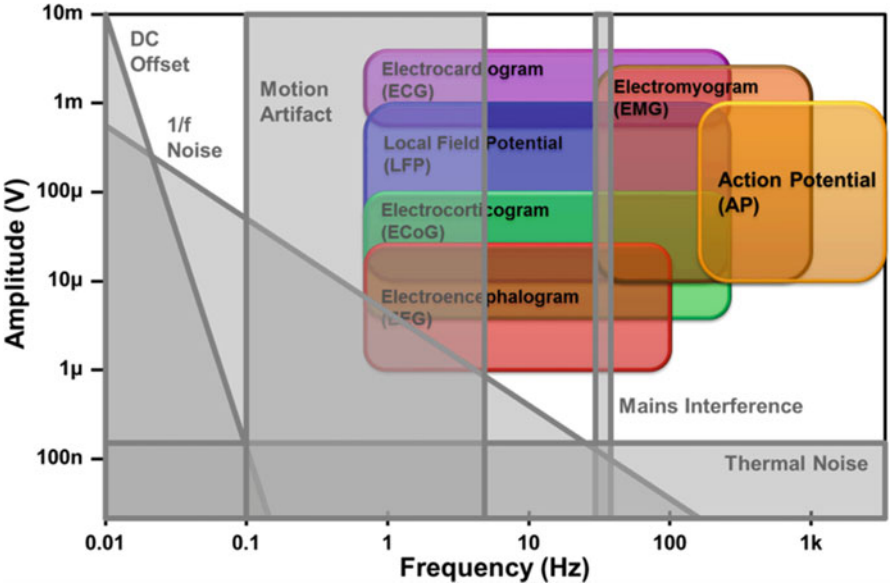

Fig. 4.8 Amplitude and frequency characteristics of various biopotential signals shown with the effect from interferences and disturbances

Table 4.1 Indoor air quality guidelines for VOCs

VOCs	Guideline values
Formaldehyde HCHO	30–120 µg/m^3 (25–100 ppb)
Acetaldehyde CH_3CHO	48 µg/m^3 (27 ppb)
Benzene C_6H_6	16–110 µg/m^3 (5–34 ppb)
Toluene $C_6H_5CH_3$	260–1092 µg/m^3 (69–290 ppb)
Ethylbenzene $C_6H_5CH_2CH_3$	1447–3880 µg/m^3 (264–892 ppb)
Xylene $C_6H_4(CH_3)_2$	870–1447 µg/m^3 (200–333 ppb)
Styrene $C_6H_5CH{=}CH_2$	30–300 µg/m^3 (7–70 ppb)
TVOC	200–3000 µg/m^3

amplitude we obtain, resulting in more relaxed requirement on the minimum detection limit. Compared to LFP and action potential (AP), the electrocardiogram (ECG) signal usually has larger amplitude because of the difference in their intrinsic signal strengths. The LFP and AP are originated from the activities of neurons in the brain, while the ECG is from the activities of electrogenic cells in cardiac muscles. Table 4.1 shows the indoor air quality guidelines especially for volatile organic compounds (VOCs) harming human health significantly. The range of guideline values covers the values used in different countries. Since the harmful effect is caused even with a very little amount of such gases, the required detection limit reaches as low as several ppb levels.

Required sensing bandwidth is mainly determined by the intrinsic signal characteristics and the distance between the signal origin and the sensing site. Except some applications sensing images and videos, the bandwidth requirement is not usually so high, but tends to be higher when the sensor is placed closer to the signal origin. For example, although neural signals such as AP, LFP, ECoG, and EEG share the same signal origin, the signal bandwidth for invasive neural recording is larger than that for non-invasive EEG recording (Fig. 4.8).

The dynamic range requirement is determined by intrinsic signal or sensor characteristics, effect from various interferences and disturbances, and the signal range of interest. For example, assume that we record the LFP and AP signals simultaneously. Since the spikes in the AP signal having an amplitude of tens or hundreds of microvolts appear on top of the LFP signal with an amplitude of a few millivolts, if an input-referred noise of 4 μV_{rms} is needed to meet the signal-to-noise ratio requirement of the spike signal recording and the LFP signal has an amplitude of 2 mV, the dynamic range requirement becomes 54 dB, resulting in about 9-bit resolution. In addition, if we consider interferences as large as a few hundreds of millivolts, the required dynamic range may reach nearly 100 dB. To avoid that, a good common-mode rejection performance needs to be guaranteed. Some sensors such as gas sensors and inertial sensors for navigation require very large dynamic range. Metal-oxide thin-film gas sensors require the interface circuit having a large dynamic range over 140 dB to accommodate high sensitivity, process spread, drift over time, and large variation in sensor resistance values for different doping types and levels used to detect different target gases. The navigation-grade accelerometer requires the dynamic range larger than 100 dB.

Aforementioned requirements on minimum detection limit, bandwidth, and dynamic range determine the necessary sensing performances and power consumption. Stringent requirements on minimum detection limit, bandwidth, and dynamic range usually lead to significant power consumption, and hence low-power circuit techniques are needed more strongly. To provide necessary performances, the sensor and its interface circuit often need to be calibrated. The calibration strategy is another important factor to consider. Especially when the application requires low-cost sensing solution, the time and effort spent for calibration should be minimized while providing necessary performance after calibration. In case of nano-scale sensors, they tend to have large variations in their characteristics at the cost of ultra-high sensitivity offered [5]. Therefore, effective and efficient calibration method has to be developed.

4.3.3 Sensing Duty Cycle

Depending on the characteristics of target physical parameters, the sensing operation can be duty-cycled to minimize the overall energy consumption as well as the amount of the data that need to be transmitted. Very low-duty-cycle sensing can be utilized when slow varying signals are monitored as in the cases of environmental

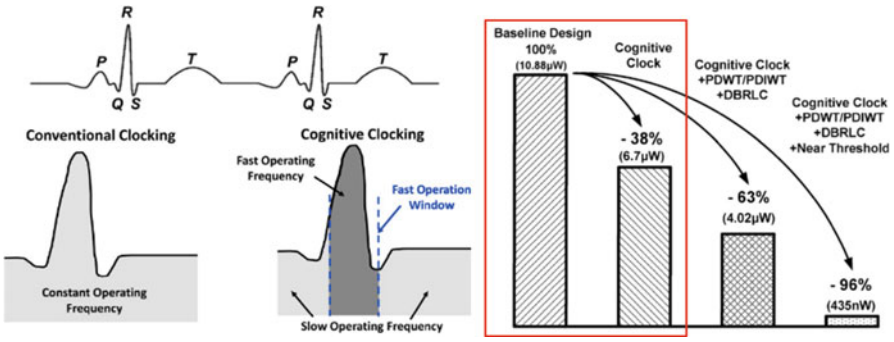

Fig. 4.9 Ultra-low-power electrocardiogram (ECG) processor employing cognitive clocking [6]

monitoring, civil structure monitoring, and progress monitoring of chronic diseases. In environmental monitoring, the sensing interval can be hours, and for intraocular pressure monitoring, the pressure may be recorded every 15 min, for example. When we sense scarce and bursty signals such as ECG signal and neural spikes, fine-grain duty cycling or adaptive operation can be employed. For example, in neural spike recording, by implementing a spike detection function, we may execute data conversion process only when spikes are detected.

Such duty-cycled sensing operation leads to reduction of average power consumption as well as sensor data. Moreover, duty cycling in sensing function does not entail any synchronization issues unlike the case of duty cycling in communication function where the synchronization between sensor nodes or between a sensor node and a host device poses a significant challenge. Figure 4.9 shows the example of adaptive or cognitive clocking scheme used for ultra-low-power ECG signal monitoring and processing [6, 7]. By using this technique, the average power consumption is reduced by 40 % without causing any timing or synchronization issues.

4.3.4 Example: Neural Recording

The example to investigate for application-dependent sensing approach is implantable neural recording and the target application is implantable neuroprobe microsystem for motor prosthesis (Fig. 4.10) [8–11]. This microsystem consists of a probe array inserted into motor cortex of human brain, a neural recording IC (IC1) which is directly integrated on the top plate of the probe array, a wireless power and data link IC (IC2) which is placed between the skull and scalp, a flexible cable connecting the neural recording IC and the wireless power and data link IC. In the microsystem, the neural recording IC working together with the probe array senses multichannel neural signals by providing functions of amplification, filtering, and digitization. This application doesn't require extremely small minimum

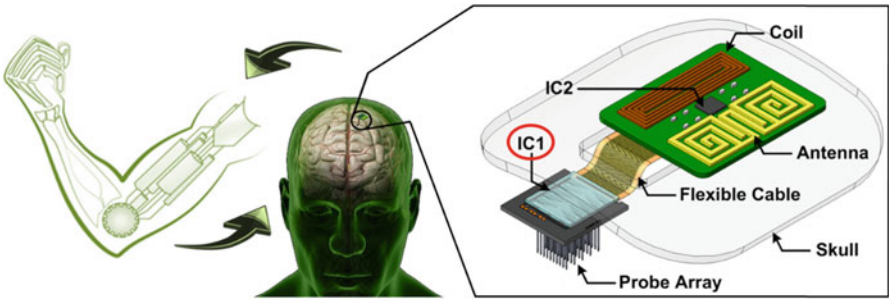

Fig. 4.10 Implantable neuroprobe microsystem for motor prosthesis

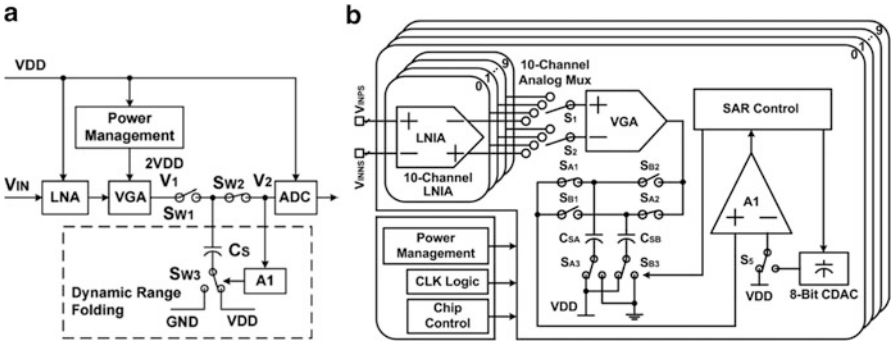

Fig. 4.11 Dual-supply ultra-low-power neural recording IC with dynamic range folding [9]: (**a**) block diagram showing only one recording channel, (**b**) block diagram of 100-channel recording IC

detection limit, as the neural spikes are recorded invasively and therefore have a relatively large amplitude. Compared to other types of neural signals, the spike signal requires a larger bandwidth of over 5 kHz and a moderate dynamic range of about 60 dB. Since the microsystem is implanted inside human body, ultra-low-power consumption should be achieved. Utilizing bursty signal characteristics of the neural spikes, duty-cycled sensing can be implemented.

4.3.4.1 Dual-Supply Ultra-Low-Power Neural Recording IC with Dynamic Range Folding

Figure 4.11a shows the block diagram of the proposed neural recording circuit for one channel [9]. It is dual-supply ultra-low-power neural recording IC with dynamic range folding. The supply voltage of 0.45 V ($=V_{DD}$) is used for the low-noise instrumentation amplifier (LNIA) as it consumes high current for low-noise operation but has low voltage swing. 0.45 V is used for the successive approximation analog-to-digital converter (SAR ADC) as well to reduce the

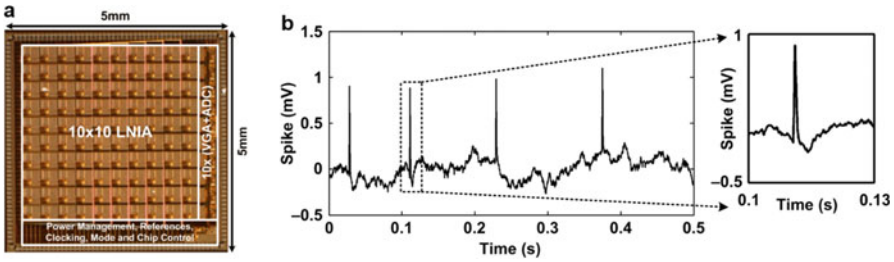

Fig. 4.12 Implementation results of the neural recording IC [9]: (**a**) microphotography of the fabricated chip, (**b**) in vivo neural signal recorded from the rat model

charging and discharging power consumed in its capacitive digital-to-analog converter (DAC) circuit and the digital switching power consumed in its control logic and register circuit. For the variable gain amplifier (VGA), as it consumes very low current but requires high voltage swing, we power this block with $2V_{DD}$ which is 0.9 V. However, we then have to resolve the mismatch in the signal dynamic range between the VGA and ADC which is caused by this dual-supply scheme. To solve this problem, a new dynamic-range-folding technique is applied and the details of this technique can be found in [8, 9]. By doing so, we could save 50 % of the power consumption without degrading noise, bandwidth, and dynamic range performances. The block diagram of the entire 100-channel neural recording IC is shown in Fig. 4.11b [9]. It consists of ten recording blocks, each of which contains ten recording channels. 10-to-1 analog multiplexer is located between ten neural amplifiers and a single VGA not only to minimize the area consumption but also to simplify the implementation of the multiplexer and the pipeline sample-and-hole network.

Figure 4.12a shows the proposed neural recording IC fabricated in 0.18-μm CMOS technology, occupying the die area of 5 × 5 mm [9]. By multiplexing before the VGA, the area consumption is saved by 22 % overall. The dual-supply scheme combined with dynamic range folding technique enabled extremely low power consumption of 730 nW/channel while providing 9-bit sensing resolution. Figure 4.12b presents the recorded in vivo neural signal, which is reconstructed from the ADC output code and scaled for input-referring [9]. The characteristic biphasic neuronal spike is indicative of a recording from the cell body of a neuron in the anterior cingulate gyrus, a region in the frontal cortex of the brain.

4.3.4.2 Ultra-Low-Power Neural Recording IC with Delta-Modulation-Based Spike Detection

Since the spikes are rare events in neural signal (10–100 fires/s typically), it is desirable to record only the spikes in order to minimize power dissipation as well as the amount of recording data to transmit while preserving the fundamental information of neuronal activities. A spike detection function can therefore be

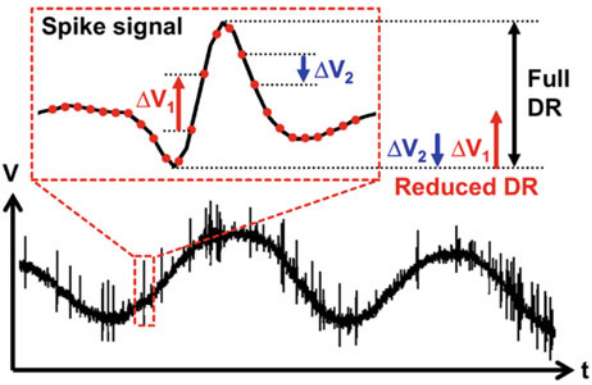

Fig. 4.13 Typical waveform of neural signal waveform (LFP and spikes), with the concept of dynamic range compression and spike detection illustrated in the inset [10]

implemented for duty cycling. Figure 4.13 presents typical neural signal waveform consisting of LFP and spikes together with the concept of delta-modulation-based spike detection [10]. For spike detection, consecutive delta values of the input signal are monitored to extract the frequency and amplitude information. By checking the polarity of the delta values continuously, too high and too low frequency components can be rejected on one hand. On the other hand, too low amplitude and too low frequency components can be ruled out by checking the size of the delta values. Using this delta-modulation-based spike detection technique, we can compress effective dynamic range and bandwidth to cover and enable fine-grain duty cycling, while preserving the neural spike waveform information.

The block diagram of the proposed 16-channel neural recording IC is depicted in Fig. 4.14 [10]. The delta modulator following a low-noise amplifier (LNA) subtracts two consecutive neural signal values so that the signal dynamic range can be reduced by half the normal range. Up to six values resulting from the subtraction in series are stored in analog first-in-first-out (FIFO) memory for a spike detector in the next stage. The detector recognizes the frequency as well as the amplitude of the signal from the stored set of several consecutive delta samples, extracting the spikes from the entire neural signal accurately. The spikes are detected during the sampling phase before the 8-bit SAR ADC operates. The ADC and transmitter (not included in this design) therefore consume power only when they process the spikes, realizing the neural recording system that runs with optimal energy efficiency.

A prototype neural recording IC with 16 channels has been fabricated using 0.18-μm CMOS technology and fully characterized. Figure 4.15a shows the micrograph of the fabricated recording chip [10]. The area of the whole chip and one recording channel is 2.35×2.5 mm and 200×800 μm, respectively. Because the delta modulator compresses the dynamic range, we can reduce 1 bit of the ADC resolution, implementing 8-bit SAR ADC. Moreover, the MSB is equivalent to the sign of the signal, and hence 7-bit capacitive DAC is sufficient to cover the entire signal range. In order to verify the spike detection functionality, in vitro test of arbitrary neural signal acquisition has been performed. We used the pre-recorded

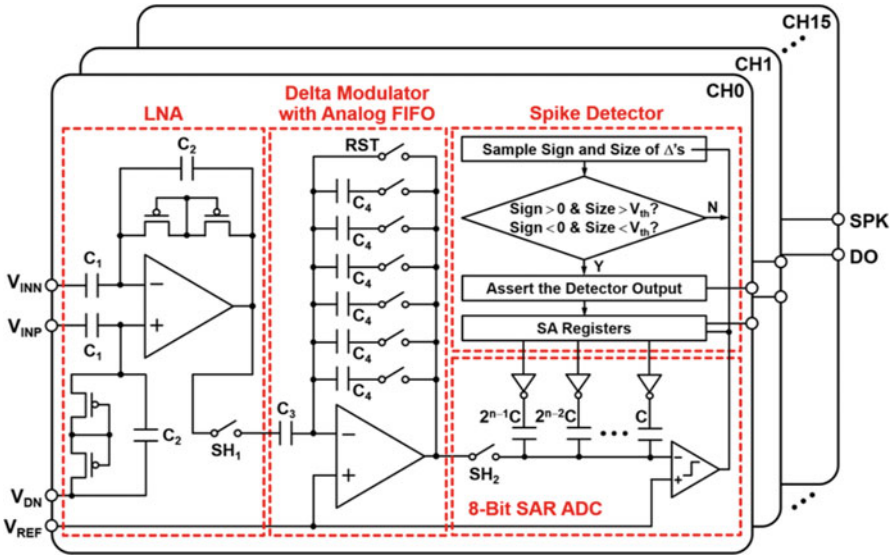

Fig. 4.14 Block diagram of the 16-channel neural recording IC with delta-modulation-based spike detection [10]

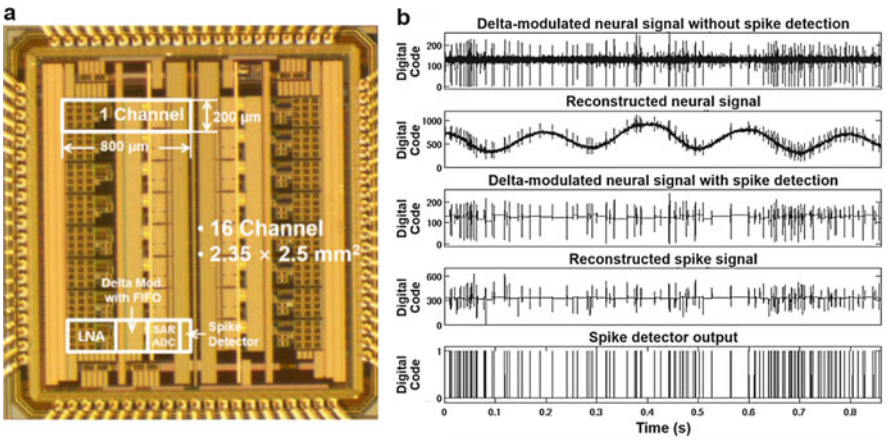

Fig. 4.15 Implementation results of the neural recording IC [10]: (**a**) microphotography of the fabricated chip, (**b**) recorded neural signal waveforms with and without activating the spike detector

neural signal provided by Plexon for the assessment of the spike detector. Figure 4.15b shows the neural signal waveforms recorded for 0.9 s with and without activating the spike detector [10]. The upper two plots are the output of the delta modulator and the reconstructed neural signal obtained by integrating the delta signal. The lower three plots show the extracted spike signal in delta values, the reconstructed spike signal, and the output of the spike detector.

4.4 Communication

4.4.1 Communication Medium

The communication medium is an application factor in the communication function. The medium used for communication is determined by the location of the physical objects where the microsystem is embedded. In most cases, communication is performed wirelessly thorough free air. However, some devices communicate through other communication media. Wearables and implants may use human body as a communication channel. Smart electricity meters may use power lines and sensors for oil exploration may use drilling pipes.

Then, in turn, the communication medium determines communication frequency, bandwidth, and achievable data rate. When we communicate through human body, the frequency band from 40 to 70 MHz as human body has bandpass characteristics. Safety is another important concern in this case. In logging-while-drilling (LWD) tools for oil well exploration, if the telemetry is implemented using electromagnetic propagation, it cannot reach more than a few kilometers and the data rate is limited to a few bits per second (b/s). If mud pulse is used for telemetry, it can reach longer distance, but the data rate is still limited to about 10 b/s. People are thus developing an ultrasound-based telemetry through the drilling pipes, which can achieve much higher data rate (well over 10 kb/s) than other approaches.

4.4.2 Example: Body-Channel Communication

By using the human body as a communication medium, the body-channel communication can achieve high energy efficiency compared to other wireless communication approaches as shown in Fig. 4.16b [13]. However, the data rate tends to be rather low, being insufficient for multimedia communication between wearable devices, such as between smart watch and smart glasses (Fig. 4.16a). A high-data-rate wideband body-channel communication transceiver therefore needs to be developed [12, 14, 15]. As mentioned in Sect. 4.4.1, the body channel has bandpass characteristics and two plots in Fig. 4.17 show such characteristics. The top figure shows the channel gain for the path A which is within one arm, and the bottom one is for the path T which is from one arm to the other across the torso.
The block diagram in Fig. 4.18a shows the structure of the wideband receiver [12]. We use tri-level direct digital Walsh-coded signaling for high data rate and high energy efficiency. To optimize the channel characteristics and achieve high data rate with limited channel bandwidth, we use high input impedance for matching and employ an equalizer in the receiver. Since the channel doesn't pass DC signal information, a transient-detection architecture is proposed using a differentiator followed by an integrator. An injection-locking-based clock recovery

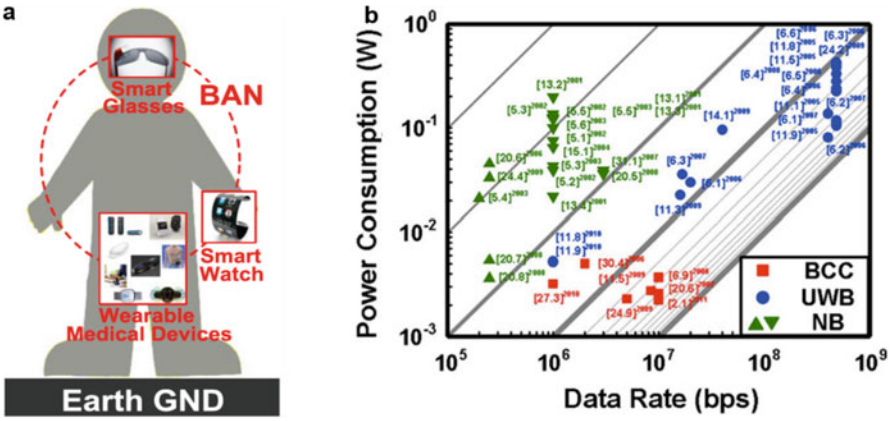

Fig. 4.16 Body-channel communication (BCC): (**a**) energy-efficient communication for wearable devices [12], (**b**) power consumption and data rate of BCC receivers in comparison with ultra-wideband (UWB) and narrow-band (NB) receivers [13]

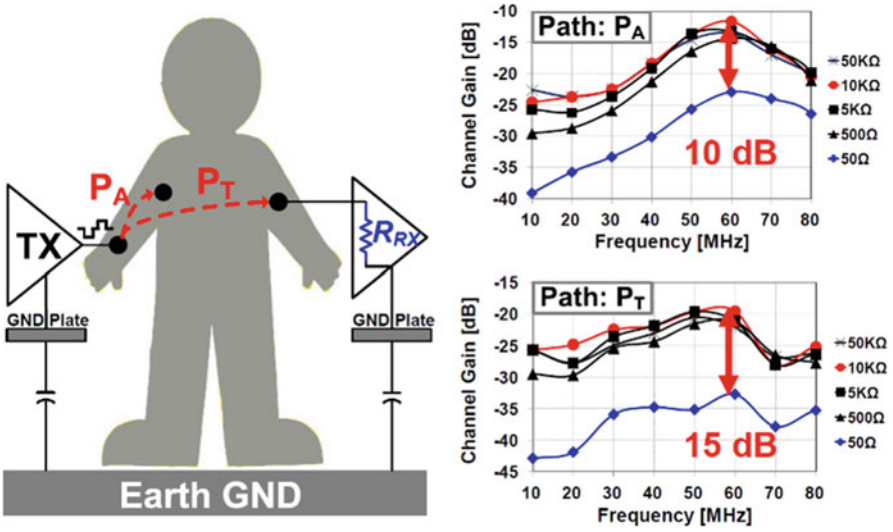

Fig. 4.17 Body-channel characteristics [12]

is also employed to provide the timing signal to the integrator and level detector, eliminating the need of a power-consuming PLL and a bulky crystal oscillator. Figure 4.18b presents the block diagram and measured output of the transmitter [12]. The transmitter consists of tri-level Walsh code modulator followed by tri-level driver. It can be seen that the dominant signal energy of the transmitter output is confined within the passband.

Figure 4.19 presents the implementation results [12]. The microphotography of the fabricated receiver and transmitter chips is shown in Fig. 4.19a. The transceiver

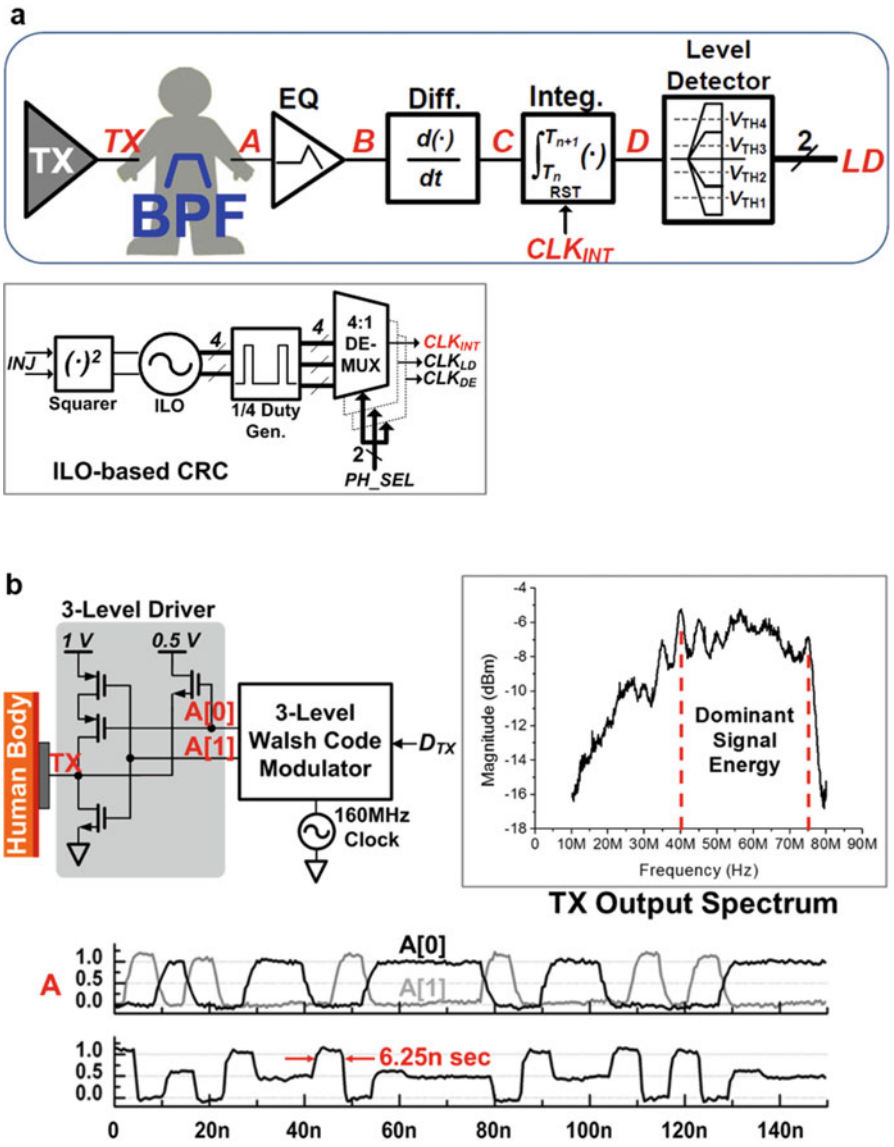

Fig. 4.18 High-energy-efficiency wideband BCC transceiver [12]: (**a**) block diagram of the receiver and clock-recovery circuit, (**b**) block diagram and measured output of the transmitter

is implemented in 65-nm CMOS process and consumes 1.85 mW in the transmitter and 9 mW in the receiver. Figure 4.19b shows the test setup and results of an image data transfer experiment. The transmitter is placed on the left arm and receiver on the right arm. The Lena image was successfully transferred in the testing.

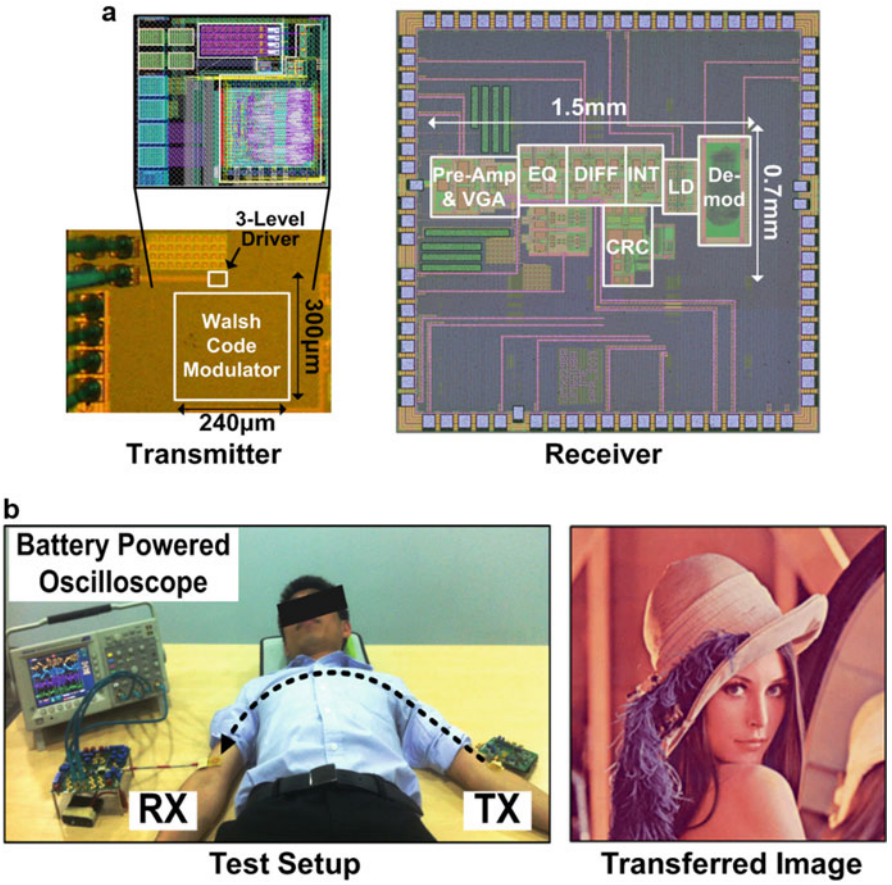

Fig. 4.19 Implementation results of the BCC transceiver ICs [12]: (**a**) microphotography of the fabricated chips, (**b**) test setup and results of an image data transfer experiment

4.4.3 Distance, Symmetry, and Protocol

Other application-dependent factors are communication distance, symmetry, and network topology. Wide-coverage sensor networks with a large number of sensor nodes require long communication distance, symmetric transceiver for multi-hop and ad-hoc communication. Such examples are smart grid and oil pipeline leak detection sensor network. On the other hand, narrow-coverage sensor networks with a small number of sensor nodes operate with short communication distance and asymmetric transceiver for master–slave communication. By doing so, the energy consumption of slave node can be minimized, while burning more power in the master side operating with sufficient energy source typically. Examples are the smart home network and body area network.

4.4.4 *Example: Wireless Capsule Endoscopy*

For wireless capsule endoscopy application (Fig. 4.20a), an asymmetric short-range transceiver is developed, together with a JPEG encoder IC [16–19]. It is for enabling the next-generation wireless capsule endoscopy, which offers high image resolution, high frame rate, and bidirectional wireless link for image transmission (uplink) as well actuator control (downlink). Considering this specific application, the transceiver has to provide high data rate to transmit high-resolution high-frame-rate images. It should consume low power so that the microsystem can operate for several hours with 2 or 3 very small coin cell batteries. To communicate through the human body with a small antenna, the communication frequency should be carefully chosen. Considering large signal attenuation at high frequencies and low antenna gain at low frequencies, 900-MHz frequency band is used in this work. Figure 4.20b shows the system block diagram of the wireless endoscopy capsule. The system has a quadrature phase-shift keying (QPSK) uplink for image transmission with 3–20-Mb/s data rate and 5–6-mW power consumption. The downlink for actuator control is based on OOK. The data rate is 500 kb/s and the power consumption is 4.5 mW. The JPEG encoder is also developed to further boost the effective data rate.

For energy-efficient implementation of the QPSK transmitter, a new injection-locking-based direct phase modulation technique is proposed [18, 19] as shown in Fig. 4.21 [16]. It changes the self-resonance frequency of a sub-harmonic injection-locked oscillator through capacitor bank switching. Since the output phase of the injection-locked oscillator is determined by the difference between the injection frequency and the self-resonance frequency, we can modulate the output phase by controlling the self-resonance frequency of the oscillator.

Figure 4.22a presents a prototype multifunctional endoscopy capsule which is built using the proposed chipset including the RF transceiver IC and JPEG encoder IC [16]. Both ICs have been fabricated in a 0.18-μm CMOS process. Their die micrographs are shown in Fig. 4.22a. The transceiver IC and JPEG encoder IC occupy the die area of 2.6×2.8 mm^2 and 2.6×2.6 mm^2, respectively. The overall

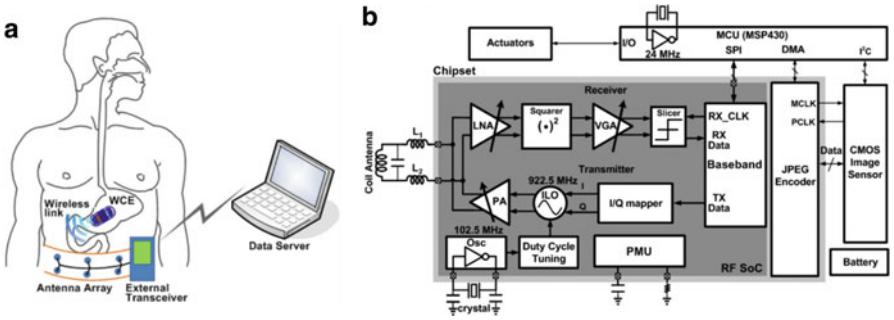

Fig. 4.20 (**a**) Wireless capsule endoscopy [16], (**b**) system block diagram of the wireless endoscopy capsule including the asymmetric short-range transceiver and JPEG encoder ICs [16]

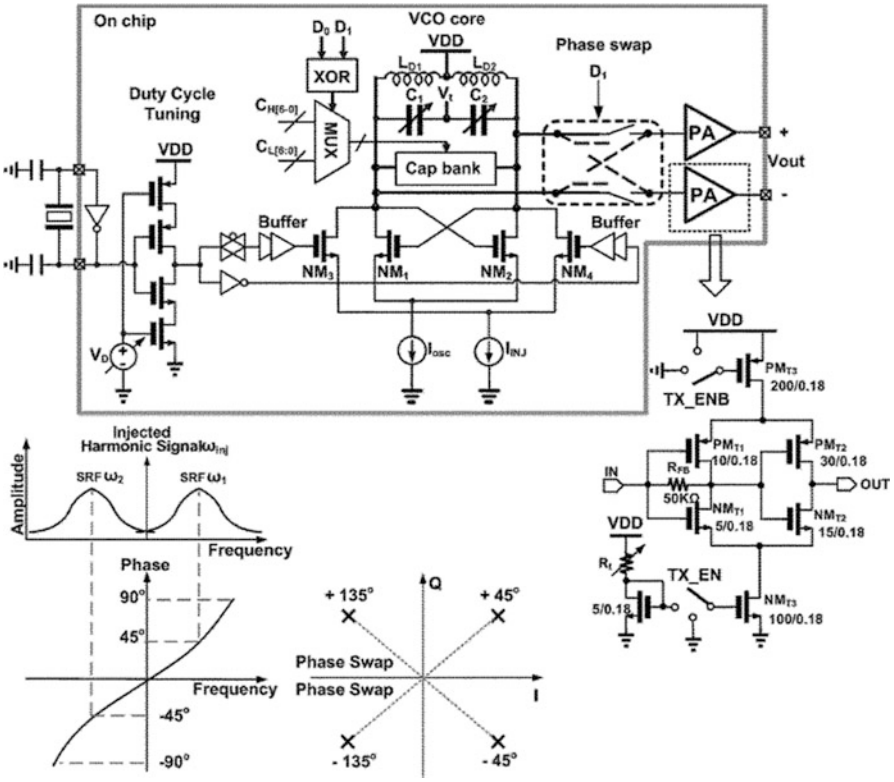

Fig. 4.21 Quadrature phase-shift keying (QPSK) transmitter design using injection-locking-based direct phase modulation [16]

capsule dimensions are 37 mm in length by 11.5 mm in diameter. About 16 % of the capsule space is reserved for a tagging actuator to cater for lesion localization. The RF transceiver, JPEC encoder, and image sensor chips are directly assembled on a rigid-flex PCB and protected by epoxy. The front and back sides of the assembled PCB system are shown in Fig. 4.22a. The full system performance has been verified by an in vivo animal experiment on porcine model as shown in Fig. 4.22b [16]. An external transceiver is implemented with discrete components. The internal images of the stomach muscle were successfully transmitted to the external receiver and displayed on the PC screen.

4.4.5 Data Rate

Being another application-dependent factor, the communication data rate is determined by the amount of sensor data to communicate. The data rate requirement is not usually so high for most of smart sensor microsystems. However, some devices

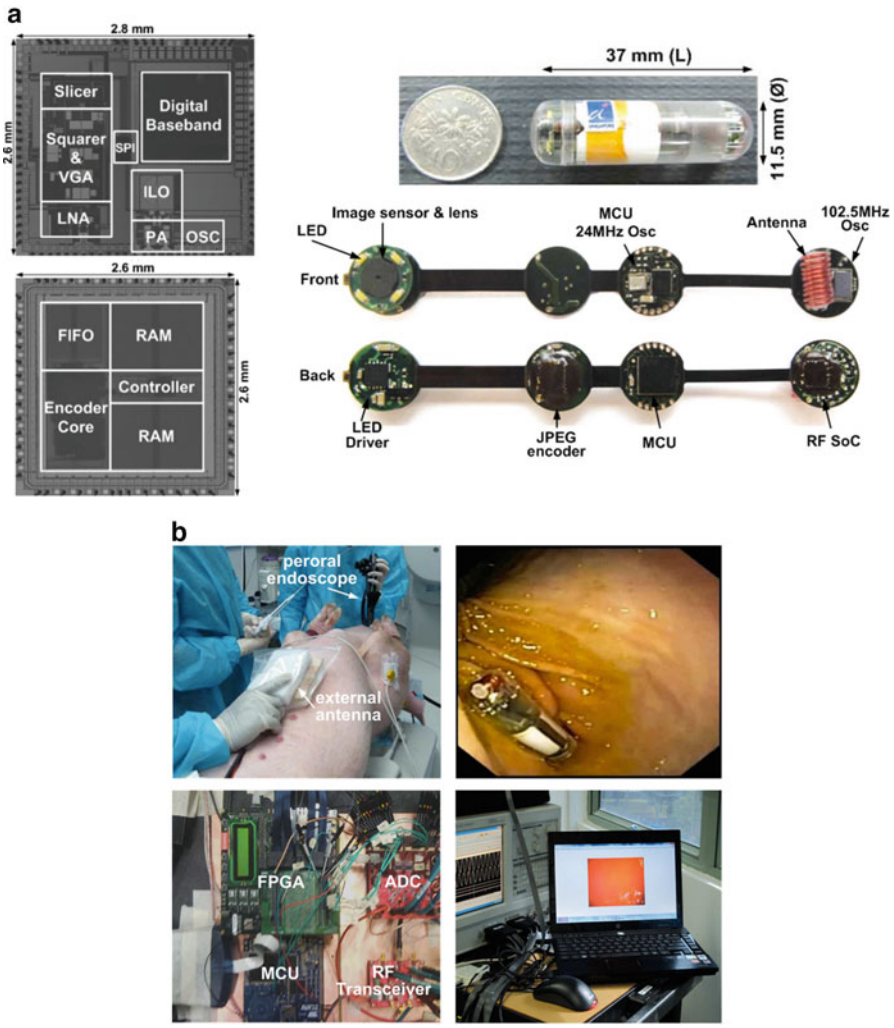

Fig. 4.22 Implementation results [16]: (**a**) chipset fabrication and microsystem integration, (**b**) test setup and results of in vivo animal experiment on porcine model

dealing with image and video data (e.g., video surveillance and capsule endoscopy) and information from large-scale sensor array (e.g., multichannel neural recording) require high-data-rate communication.

4.4.6 Communication Duty Cycle

The communication duty cycle is determined by characteristics of sensed physical parameters and usage scenario. Since the communication transceiver is usually the most power hungry block in wireless sensor microsystems, a significant amount of

energy can be saved by duty cycling the communication function. However, it entails synchronization issues, which can be mitigated by using a low-power high-accuracy clock generator, a low-power wake-up receiver, or a combination of both.

4.5 Conclusion

Unlike PC and mobile phone platforms, the smart sensor platform is used to virtualize physical objects and bring them into the networked cyber world. It therefore has so many different applications, which lead to different approaches for designing and implementing smart sensor microsystems. For different application, different strategies for sensing, processing, communication, powering, and microsystem integration are employed to provide optimum solutions.

For IC designers, it's an important prerequisite to have a good understanding of the applications where the designed circuits and systems are deployed. While improving circuit-level techniques on one hand, optimally crafting system designs on the other hand can draw the maximum out of currently available technologies. As a result, IC designers become more and more like solution providers who develop the best solutions for the problems posed by specific applications, leveraging state-of-the-art IC design techniques.

Acknowledgments This work is supported by the Center for Integrated Smart Sensors funded by the Ministry of Science, ICT and Future Planning as the Global Frontier Project.

References

1. Boisseau S, Despesse G, Ahmed Seddik B (2012) Electrostatic conversion for vibration energy havesting. In: Lallart M (ed) Small-scale energy harvesting. InTech, Chapter 5, p 92
2. Cheong JH, Ho CK, Ng SSY, Xue R-F, Cha H-K, Khannur PB, Liu X, Lee AA, Endru FN, Park W-T, Lim LS, He C, Je M (2012) A wirelessly powered and interrogated blood flow monitoring microsystem fully integrated with a prosthetic vascular graft for early failure detection. IEEE Asian solid-state circuits conference digest of technical papers, Nov 2012, p 177–180
3. Cheong JH, Ng SSY, Liu X, Xue R-F, Lim HJ, Khannur PB, Chan KL, Lee AA, Kang K, Lim LS, He C, Singh P, Park W-T, Je M (2012) An inductively powered implantable blood flow sensor microsystem for vascular grafts. IEEE Trans Biomed Eng 59(9):2466–2475
4. Khannur PB, Chan KL, Cheong JH, Kang K, Lee AA, Liu X, Lim HJ, Ramakrishna K, Je M (2010) A 21.6μW inductively powered implantable IC for blood flow measurement. IEEE Asian solid-state circuits conference digest of technical papers, Nov 2010, p 9–5
5. Chai KTC, Choe K, Bernal OD, Gopalakrishnan PK, Zhang G-J, Kang TG, Je M (2010) A 64-channel readout ASIC for nanowire biosensor array with electrical calibration scheme. Proceedings of annual international conference of the IEEE engineering in medicine and biology society, Sept 2010, p 3491–3494

6. Liu X, Zhou J, Yang Y, Wang B, Lan J, Wang C, Luo J, Goh WL, Kim TT-H, Je M (2014) A 457 nW near-threshold cognitive multi-functional ECG processor for long-term cardiac monitoring. IEEE J Solid State Circuits 49(11):2422–2434
7. Liu X, Zhou J, Yang Y, Wang B, Lan J, Wang C, Luo J, Goh WL, Kim TT-H, Je M (2013) A 457-nW cognitive multi-functional ECG processor. IEEE Asian solid-state circuits conference digest of technical papers, Nov 2013, p 141–144
8. Han D, Zheng Y, Rajkumar R, Dawe GS, Je M (2013) A 0.45 V 100-channel neural-recording IC with sub-μW/channel consumption in 0.18 μm CMOS. IEEE Trans Biomed Circ Syst 7 (6):735–746
9. Han D, Zheng Y, Rajkumar R, Dawe G, Je M (2013) A 0.45V 100-channel neural recording IC with sub-μW/channel consumption in 0.18μm CMOS. IEEE international solid-state circuits conference digest of technical papers, Feb 2013, p 290–291
10. Kim S-J, Liu L, Yao L, Goh WL, Gao Y, Je M (2014) A 0.5-V sub-μW/channel neural recording IC with delta-modulation-based spike detection. IEEE Asian solid-state circuits conference digest of technical papers, Nov 2014, p 189–192
11. Cheng K-W, Zou X, Cheong JH, Xue R-F, Chen Z, Yao L, Cha H-K, Cheng SJ, Li P, Liu L, Andia L, Ho CK, Cheng M-Y, Duan Z, Rajkumar R, Zheng Y, Goh WL, Guo Y, Dawe G, Park W-T, Je M (2012) 100-channel wireless neural recording system with 54-Mb/s data link and 40%-efficiency power link. IEEE Asian solid-state circuits conference digest of technical papers, Nov 2012, p 185–188
12. Lee J, Kulkarni VV, Ho CK, Cheong JH, Li P, Zhou J, Toh WD, Zhang X, Gao Y, Cheng KW, Liu X, Je M (2014) A 60Mb/s wideband BCC transceiver with 150pJ/b RX and 31pJ/b TX for emerging wearable applications. IEEE international solid-state circuits conference digest of technical papers, Feb 2014, p 498–499
13. Bae J, Song K, Lee H, Cho H, Yoo H-J (2012) A 0.24-nJ/b wireless body-area-network transceiver with scalable double-FSK modulation. IEEE J Solid State Circuits 47(1):310–322
14. Ho CK, Cheong JH, Lee J, Kulkarni V, Li P, Liu X, Je M (2014) High bandwidth efficiency and low power consumption Walsh code implementation methods for body channel communication. IEEE Trans Microwave Theory Tech 62(9):1867–1878
15. Kulkarni VV, Lee J, Zhou J, Ho CK, Cheong JH, Toh W-D, Li P, Liu X, Je M (2014) A reference-less injection-locked clock-recovery scheme for multilevel-signaling-based wideband BCC receivers. IEEE Trans Microwave Theory Tech 62(9):1856–1866
16. Gao Y, Cheng S-J, Toh W-D, Kwok Y-S, Tan K-CB, Chen X, Mok W-M, Win H-H, Zhao B, Diao S, Cabuk A, Zheng Y, Sun S, Je M, Heng C-H (2013) An asymmetrical QPSK/OOK transceiver SoC and 15:1 JPEG encoder IC for multifunction wireless capsule endoscopy. IEEE J Solid State Circuits 48(11):2717–2733
17. Gao Y, Cheng S-J, Toh W-D, Kwok Y-S, Tan K-CB, Chen X, Mok W-M, Win H-H, Zhao B, Diao S, Cabuk A, Zheng Y, Sun S, Je M, Heng C-H (2012) An asymmetrical QPSK/OOK transceiver SoC and 15:1 JPEG encoder IC for multifunction wireless capsule endoscopy. IEEE Asian solid-state circuits conference digest of technical papers, Nov 2012, p 341–344
18. Diao S, Zheng Y, Gao Y, Cheng S-J, Yuan X, Je M, Heng C-H (2012) A 50-Mbps CMOS QPSK/O-QPSK transmitter used in endoscopy by employing injection locking for direct modulation. IEEE Trans Microwave Theory Tech 60(1):120–130
19. Diao S, Zheng Y, Gao Y, Yuan X, Je M, Heng C-H (2010) A 5.9mW 50Mbps CMOS QPSK/O-QPSK transmitter employing injection locking for direct modulation. IEEE Asian solid-state circuits conference digest of technical papers, Nov 2010, p 1–2